Boundary-Layer Meteorology (2024) 190:32
https://doi.org/10.1007/s10546-024-00873-x

RESEARCH ARTICLE

Rainfall Effects on Atmospheric Turbulence and Near-Surface Similarities in the Stable Boundary Layer

Abdullah Bolek[1] · **Firat Y. Testik**[1,2]

Received: 16 November 2023 / Accepted: 26 June 2024 / Published online: 13 July 2024

Abstract

Near-surface similarities and atmospheric turbulence characteristics have a large impact on numerical weather prediction models. However, the validity of these similarities is unclear during precipitation. This study investigates the modulations in atmospheric boundary layer turbulence and the variations of the near-surface scaling similarities caused by rainfall. Here we present our field observations on the effects of rainfall on the near-surface similarities and atmospheric turbulence in the stable boundary layer using a Parsivel^2 disdrometer and a 3D ultrasonic anemometer at our outdoor rainfall laboratory in San Antonio, Texas, USA. During moderate to heavy rainfall conditions, higher turbulent energy was observed than those in non-rainy conditions when the turbulence intensity and the wind speeds were relatively low. On the contrary, when the turbulence intensity and the wind speeds were relatively high, the turbulence energy in the stable boundary layer were dampened due to the raindrops. Raindrops with high particle Reynolds numbers ($Re_p = D_m v_t / \vartheta$; D_m—mean volume diameter, v_t—terminal raindrop fall speed, and ϑ—kinematic viscosity of the surrounding air) can act as either a source or a sink of turbulent kinetic energy depending on the turbulence intensity of the atmosphere. Our field observations showed that near-surface similarities deviated from the scaled similarities under the influence of rainfall. The normalized standard deviations of the streamwise and vertical velocity components and the dissipation rate were higher during rainy than non-rainy times. Rainfall effects on turbulence modulations and near-surface scaling parameters of the stable boundary layer are discussed with considerations of the relevant mechanisms.

Keywords Stable boundary layer turbulence · Rainfall · Turbulence attenuation and augmentation · Near-surface similarities

---

✉ Firat Y. Testik
Firat.Testik@utsa.edu

[1] School of Civil and Environmental Engineering, and Construction Management, University of Texas at San Antonio, San Antonio, TX 78249, USA

[2] Department of Mecxhanical Engineering, University of Texas at San Antonio, San Antonio, TX 78249, USA

1 Introduction

The atmospheric boundary layer (ABL) turbulence plays a key role in many meteorological and hydrological applications including atmospheric particle dispersion, weather forecasting, wind turbine characteristics, urban meteorology, and hydrology (Garratt 1994; Kaimal and Finnigan 1994; Foken and Napo 2008; Högström 1996). Furthermore, the predictions of rainfall and convective cloud developments by Numerical Weather Prediction (NWP) models depend on how the boundary layer fluxes such as momentum, heat, and moisture are represented in the developed numerical schemes (Qian et al. 2016). The boundary layer turbulence and these fluxes under different circumstances including stable, unstable, and neutral conditions have been widely investigated (Wyngaard and Coté 1971; Kaimal et al. 1972; Dyer 1974; Kaimal 1978; Højstrup 1981; Hogstrom 1988; Kaimal and Wyngaard 1990; Pahlow et al. 2001; Oncley et al. 1996; Albertson et al. 1997; Chamecki and Dias 2004), and Monin–Obukhov Similarity Theory (MOST) is mainly used to model surface fluxes under these conditions. Although the universal applicability of the MOST is still a topic of debate (Grachev et al. 2013, 2016; Stiperski and Calaf 2018; Stiperski et al. 2019), the small-scale processes of the near-surface fluxes of momentum, heat, and moisture cannot be completely resolved in NWP models due to the large-scale nature of the problem. Therefore, in NWP models, these surface-layer fluxes need to be modeled using surface-layer schemes (Janjić 1994; Beljaars 1995). However, the validity of these surface similarities and atmospheric turbulence characteristics under rainfall has not received much attention.

The phenomenon of turbulence modulation by particles has been widely investigated (Hestroni 1989, Gore and Crowe 1991, Fessler and Eaton 1999, Ferrante and Elghobashi 2003, Bagchi and Balachandar 2004, Hwang and Eaton 2006, Balachandar and Eaton 2010, Lucci et al. 2010 and 2011, Dodd and Ferrante 2016, Rosti et al. 2019, Crialesi-Esposito et al. 2021). The turbulence energy of the carrier fluid may be either attenuated or augmented due to the presence of particles. However, the mechanisms for attenuation and augmentation are still ambiguous, and there are knowledge gaps, especially in understanding the kinetic energy budget of the turbulence and the impact of the surface tension force when the particles are liquid or gas (i.e., droplet, bubble) (Rosti et al. 2019). Gore and Crowe (1991) suggested that the ratio of the particle diameter (D) to fluid integral length scale (l) is the determining factor of turbulence modification, and they noted that turbulence is enhanced for $D/l > 0.1$ and suppressed for $D/l < 0.1$. On the other hand, Hestroni (1989) related turbulence modulations primarily to the particle Reynolds number ($\mathrm{Re_p} = \mathrm{D_m v_t}/\vartheta$; $\mathrm{D_m}$—mean volume diameter, $\mathrm{v_t}$—terminal raindrop fall speed, and ϑ—kinematic viscosity of the surrounding air) and proposed that the particles with high particle Reynolds number ($Re_p > 400$) augment the turbulence due to vortex shedding, whereas particles with low $\mathrm{Re_p}$ tend to suppress the turbulence by absorbing energy. Later, Bagchi and Balachandar (2004) discussed the intricate relationship among the carrier fluid turbulence levels, wake oscillations, and vortex-shedding processes in determining turbulence attenuation and augmentation. Bagchi and Balachandar showed that while the wake oscillations and vortex shedding of particles at low turbulence intensity levels of the carrier fluid cause turbulence augmentation, at high turbulence levels of the carrier fluid the interferences between the carrier fluid turbulence and wake processes may lead to turbulence attenuation or marginal augmentation. In more recent studies, the mechanisms that attenuate the carrier fluid turbulence were related to the increased turbulent kinetic energy dissipation rate (ε) due to an increase in the magnitude of the velocity gradients near the particle or droplet surface (Lucci et al. 2010; Dodd and Ferrante 2016; Rosti et al. 2019). Rosti et al. (2019) further suggested a phenomenon called the blocking effect in determining turbulence modulations, which causes abrupt re-orientation of the turbulent eddies in the carrier fluid flow. This process causes increases in both turbulent production and dissipation rates due to an increase in the magnitude of the Reynolds stress when particles are present.

Caldwell and Elliott (1972) found that rainfall with a rainfall rate (R) of about 30 mm hr^{-1}, while not having a notable impact on the wind speed, enhances the shear stress in the air by about 10–15%. On the contrary, Aylor and Ducharme (1995) found similar turbulent characteristics during rainy and non-rainy weather conditions from near ground (a few meters above ground) measurements for R values less than 7.2 mm hr^{-1}. More recently, Harrison et al. (2012) found that rainfall (R ~ 30 and 60 mm hr^{-1}) under low wind speed conditions enhances friction velocity (u_*) for the given wind speed. It is, therefore, important to understand the effects of raindrops on the stable boundary layer (SBL) turbulence characteristics and test the near-surface scaled similarities during rainfall.

In this study, the effects of rainfall on atmospheric turbulence characteristics and near-surface similarities were investigated by in-situ measurements. Here, we consider only the SBL conditions for which the vertical mixing is relatively low; hence, the effects of rainfall are expected to be more pronounced. Rainfall microphysical and bulk characteristics were collected by using an OTT Parsivel^2 disdrometer, whereas the atmospheric turbulence statistics were calculated using the wind measurements of a 3D ultrasonic anemometer. Section 2 provides details on our field site and instrumentation, pre-processing of collected data to ensure data quality, and near-surface similarity scaling relationships. In Sect. 3, the effect of raindrops on turbulence modulation and the applicability of the scaling relationships during rainfall are presented. Finally, conclusions are provided in Sect. 4.

2 Field Site and Methodology

2.1 Field Site and Instrumentation

In-situ measurements of rainfall and atmospheric turbulence characteristics were performed (during 26 different rainfall events) between May 2019 to October 2021. Additional wind measurements were conducted under non-rainy conditions to compare the turbulence statistics (during 13 different non-rainy times). The field site is located at the West Campus of the University of Texas at San Antonio with the coordinates 29°34′43.37″ N, 98°37′49.90″ W, and elevation 296 m above sea level. The field site is surrounded by sparsely distributed short trees and vegetation with a maximum height of 5 m (for details about the field site, see Bolek and Testik 2021, Testik and Bolek 2023, and Saha and Testik 2023).

An OTT Parsivel^2 disdrometer, installed on top of a 2 m high pole, was used to collect rainfall microphysical and bulk characteristics including raindrop diameter (D), fall speed (V_f), and rainfall rate (R) (see Fig. 1a and b). Saha and Testik (2023) provide a description of the Parsivel^2 disdrometer setup at our field site and the results of a detailed investigation on its algorithm and measurement accuracy. Parsivel^2 disdrometer consists of a laser sensor that forms a light sheet between its transmitter and receiver units. The amount of light that is captured by the receiver depends on the size of the hydrometeors, while the fall speed of the hydrometeors is correlated with the passage time of the hydrometeors through the light sheet. Parsivel^2 measures the raindrop D and V_f in 32 non-equidistant bin sizes for each parameter, which range from 0.062 to 25 mm for D and 0.05 to 20 m s^{-1} for V_f. The measurement accuracies of Parsivel^2 for D and V_f are ± 1 size class for drops that are $0.2 < D < 2.0$ mm

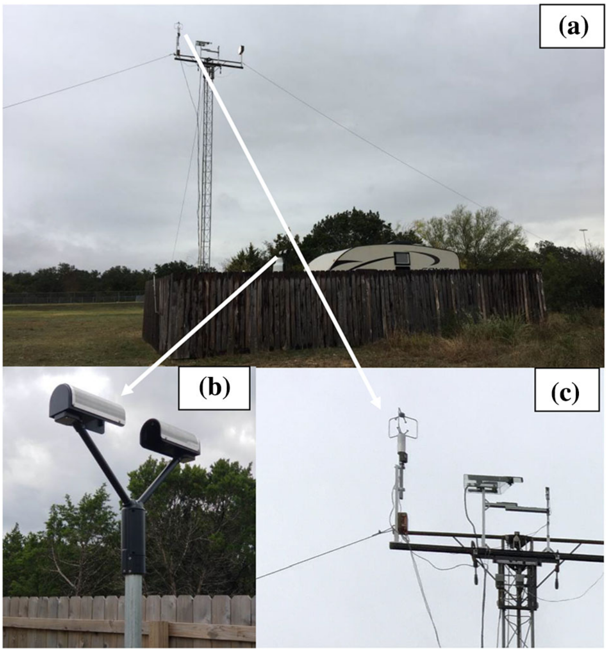

Fig. 1 Photographs showing: **a** the field site with instruments deployed, **b** Parsivel^2 disdrometer on top of the 2 m-high pole, and **c** RM-Young 81,000 anemometer on top of the 10 m-high meteorological tower

and ± 0.5 size class for drops that are $D > 2.0$ mm. These correspond to accuracy ranges of 0.125 to 0.5 mm for D and 0.1 to 0.8 m s^{-1} for V_f for drops that are $D < 10$ mm. The measurement accuracy of Parsivel^2 for R is 5%. Detailed information on D and V_f bins and measurement accuracy is available by OTT-Hydromet (2017).

A 3-D ultrasonic anemometer (RM-Young 81,000), mounted on top of a 10 m tall meteorological tower, was used to quantify the surface layer turbulence characteristics (see Fig. 1 a and c; see also Testik and Bolek 2023). The anemometer was set to sample wind data at 32 Hz. The measurement accuracy of the instrument is provided by the manufacturer as ± 1% for wind speeds between 0–30 m s^{-1} and ± 3% for wind speeds between 30–40 m s^{-1}.

2.2 Preprocessing

Parsivel^2 provided data for rainfall rate R and fall speed V_f and diameter V of all raindrops observed during each minute in 1 min data intervals. We used Eq. (1) and raw Parsivel^2 data for D and V_f (see Saha and Testik 2023) to calculate the average raindrop diameter ($\overline{\mathrm{D}}$) in mm for every minute. We also calculated the mean (D_m, Eq. 2) and median (D_0, Eq. 3) raindrop volume diameter in mm from Parsivel^2 raindrop size distribution $N(D)$ output (K'ufre-Mfon et al. 2015):

$$\overline{D} = \frac{1}{N}\sum_{n=1}^{N} D_n, \tag{1}$$

$$D_m = \frac{\int D^4 N(D)dD}{\int D^3 N(D)dD}, \tag{2}$$

$$D_0 = \frac{3.67 + \mu}{4.0 + \mu} D_m. \tag{3}$$

Here, μ is the shape parameter in gamma raindrop size distribution (DSD) and is considered as 0.86 in our calculations following Ryzhkov and Zrnic (2019). Park et al. (2017) reported significant bias in Parsivel^2 data for rainfall events with $D_m > 2.0$ mm. In this study, we used the data corresponding to D_m values smaller than 3.0 mm and disregarded the data corresponding to D_m values larger than 3.0 mm due to potential bias in Parsivel^2 measurements. This extension of the D_m limit from 2.0 mm to 3.0 mm was to not discard all the intense rainfall events while limiting the instrumental bias to a certain degree.

Wind measurements, data processing, and calculations of turbulence quantities are described in Testik and Bolek (2023) in detail and are briefly described here for completeness. We used a spike removal algorithm to eliminate unphysical spikes which occur due to water accumulation on the transducer face (Aylor and Ducharme 1995; Vickers and Mahrt 1997). The double coordinate rotation procedure (Wilczak et al. 2001) was employed to align the horizontal wind to the streamwise component and reduce the effect of terrain slope from the vertical wind velocity component. Note that Zhang et al. (2016), studying the effects of precipitation on sonic anemometer measurements of turbulent fluxes in the atmospheric surface layer, showed that the spectra of wind velocity and co-spectra of momentum flux calculated using sonic anemometer measurements were not sensitive to the presence of raindrops. Zhang et al. showed that these spectra resemble the universal shape and slopes at the inertial subrange even under heavy precipitation conditions. However, they found that sonic temperature measurements were sensitive to precipitation, presumably due to changes of the medium from air to air with liquid water between the transducers. Therefore, in our study, the temperature measurements of the anemometer were not used for in-depth analysis, except for calculating the Obukhov length to specify the stability of the boundary layer and the heat flux to remove non-stationary data.

Streamwise velocity component consists of an average and fluctuating component:

$$u = u' + \overline{u}. \tag{4}$$

Here, u is the instantaneous streamwise component of the wind velocity, overbar represents averaged, and prime denotes the fluctuating component. The averaging time was selected as 1-min for turbulence calculations. This averaging time was selected to avoid the fluctuations caused by (sub-)mesoscale motion and it has been used previously by various studies for SBL (Mahrt et al. 2015; Kit et al. 2017; Stiperski and Calat 2018; Stiperski et al. 2019; Conry et al. 2020; Boyko and Vercauteren 2021). Furthermore, we implemented the instationarity test described by Foken and Wichura (1996) to disregard the data that potentially reflects mesoscale fluctuations. In this test, if the difference between the covariance value for the full period and the mean covariance of the intervals of select size for this period is less than 30%, the measurement is considered to be stationary. When implementing this test and calculating the momentum and heat fluxes in our study, we used 30 min as the full period and 1 min as the interval size. Accordingly, for any given 30 min dataset, if there was more than 30% difference between the flux value calculated using a 30 min averaging window and the mean of the 30 flux values calculated using a 1-min averaging window within the same period, then the 30 min dataset was removed from analyses (see Foken and Wichura 1996 for details). In this study, the stability condition for the boundary layer was set as $0 < z/L < 10$, where z/L is the Monin–Obukhov stability parameter (z—measurement height and L—Obukhov length scale as defined in Eq. 9 later) and its values of 0 and 10 represent neutral and very stable boundary conditions, respectively. Our observational data falling outside of the $0 < z/L < 10$

range were disregarded from further analyses. We further removed data from analyses for wind speeds less than 0.1 m s^{-1} and also for turbulent intensity values (defined in Eq. 5) larger than 0.5 based on applicability considerations for Taylor's frozen turbulence hypothesis (Pahlow et al. 2001):

$$TI = \sigma_{u'}/\overline{u}. \tag{5}$$

Here, σ denotes the standard deviation of the streamwise velocity fluctuation. Turbulent kinetic energy (k) was calculated as given in Eq. (6):

$$k = 0.5\left(\overline{(u')^2} + \overline{(v')^2} + \overline{(w')^2}\right), \tag{6}$$

where v and w are the lateral and vertical components of the wind velocity. Finally, the data were omitted when the fractional difference between the calculated dissipation rate by using the second-order structure function ($\varepsilon_{\mathrm{SSF}}$) and spectral fitting (often referred to as the inertial range method, $\varepsilon_{\mathrm{IRM}}$) was higher than O(1). Since both methods use Kolmogorov's inertial range theory either in frequency (ε_{IRM}, $n^{-5/3}$, where n is frequency) or in the time domain (ε_{SSF}, $\zeta^{2/3}$, ζ is time separation), this criterion is expected to further restrict the data and reduce the excessive scatter that is generally observed in SBL. The ε_{IRM} was calculated using the 1-D streamwise turbulent energy spectra ($S_u(n)$) given in Eq. (7):

$$\varepsilon_{IRM} = \frac{2\pi}{\overline{u}}\left(\frac{n^{5/3}S_u(n)}{\alpha_u}\right)^{1.5}. \tag{7}$$

Here in our calculations, the selected value of α_u, denoting the Kolmogorov constant, was 0.52. The parameter of $n^{5/3}S_u(n)$ was calculated as the average of the maximum and adjacent two points with 0.5 Hz intervals among the frequency bands from 0.5 to 4 Hz (Oncley et al. 1996). For ε_{SSF} calculations, Eq. (8) was used:

$$\varepsilon_{SSF} = \frac{1}{\overline{u}\zeta}\left(\frac{D_u(\zeta)}{C_k}\right)^{1.5}. \tag{8}$$

Here, $D_u(\zeta) = \overline{[u'(t+\zeta) - u'(t)]^2}$ is the streamwise second-order temporal structure function with the time separation of ζ, which approximates the streamwise second-order structure function at separation $\overline{u}\zeta$ by Taylor's hypothesis, and $C_k \approx 2.0$ is the Kolmogorov constant. In this study, the range of ζ was chosen as 0.1–2 s for the computations since the structure function and Kolmogorov's inertial range slope (in the time domain) $\zeta^{2/3}$ was in good agreement, and this range was used in previous studies (Muñoz-Esparza et al. 2018; Bodini et al. 2018, 2019; Testik and Bolek 2023). Note that ε_{SSF} was used for the rest of the paper and it is, henceforth, denoted as ε. The ranges of the observed turbulence characteristics and R throughout this study for $0 < z/L < 10$, and $R > 2.6$ mm hr^{-1} are given in Table 1. In this study, rainy times were defined as $R > 2.6$ mm hr^{-1}, which is the limit of moderate rainfall. Taylor Reynolds number (Re_λ) was calculated as $Re_\lambda = \sqrt{20k^2/3\varepsilon\vartheta}$, l is the integral length scale and was calculated using the autocorrelation coefficient, l_η is the Kolmogorov length scale that was calculated as $l_\eta = \left(\vartheta^3/\varepsilon\right)^{0.25}$, and u_* is the friction velocity calculated using Eq. 10 provided later. From Table 1, it can also be seen that the ranges of the mean wind speed for the rainy and non-rainy conditions have a large difference. In presenting the results, data was binned by either using the mean wind speed or the stability parameter. Binning the data ensured comparisons between similar conditions, avoiding substantial biases. Throughout this study, a total of 4197 min of rainy wind data and 1280 min of non-rainy wind data

Table 1 The ranges (minimum–maximum) of observed turbulence characteristics and rainfall rates for $0 < z/L < 10$ for rainy ($R >$ 2.6 mm hr^{-1}) and non-rainy ($R = 0$) events throughout this study

	$R > 2.6$ mm hr^{-1}	$R = 0$
$\overline{u}$	0.5–12.4 m s^{-1}	0.56–7.01 m s^{-1}
u_*	0.053–1.85 m s^{-1}	0.034–1.3 m s^{-1}
Re_λ	675–11,765	398–6910
l	0.8–76.6 m	0.52–57.8 m
l_η	0.23–2.0 mm	0.33–1.7 mm
R	2.61–120 mm hr^{-1}	–

were collected. At the end of this preprocessing and quality criteria, 63 and 76% of the rainy and non-rainy 1 min dataset were eliminated, respectively, and 1547 and 309 1 min data were used, respectively, to calculate turbulence characteristics for the rest of this paper. Although the size of the remaining data is relatively small, it is sufficient for the validity of the results drawn in this study. The stringent data quality criteria applied to the collected data ensured that the results were from a data set that was representative of the relevant processes. Furthermore, the statistical significance of the results was tested and verified for the relevant analyses.

2.3 Similarity Scaling

For modeling of the SBL near-surface similarities, numerical weather prediction models generally use MOST with the stability parameter z/L, where L can be calculated by Eq. (9):

$$L = \frac{-u_*^3\overline{\theta}}{\kappa_c g \overline{w'\theta'}}. \tag{9}$$

Here, $\overline{\theta}$ is the 1 min averaged sonic temperature and κ_c is the von Karman constant that is approximately equal to 0.4. Note that, here we used sonic temperature instead of virtual potential temperature due to lack of moisture measurements, which was expected to result in less than about 5 and 10% uncertainty in temperature variance and heat flux calculations, respectively (Liu et al. 2001). Here, u_* is the friction velocity and was calculated by Eq. (10):

$$u_* = \sqrt[4]{\left(\overline{u'w'}\right)^2 + \left(\overline{v'w'}\right)^2}. \tag{10}$$

According to MOST, the standard deviations of the wind velocity ($\sigma_{u,w}$) can be scaled by using u_*. Here we used the scaling similarity relationships for the standard deviations of the wind velocity ($\Phi_{u,w}$) in stable stratification by Stiperski et al. (2019):

$$\Phi_u = \frac{\sigma_u}{u_*} = 2.55(1 + 3(z/L))^{1/3}, \tag{11}$$

$$\Phi_w = \frac{\sigma_w}{u_*} = 1.25(1 + 3(z/L))^{1/3}. \tag{12}$$

Finally, MOST similarity relationships for ε in stable stratification Φ_ε by Grachev et al. (2016) and Wyngaard and Cote (1971) were used (Eqs. 13 and 14, respectively):

$$\Phi_\varepsilon = \frac{\kappa_c z \varepsilon}{u_*^3} = 1 + 5.2(z/L), \tag{13}$$

$$\Phi_\varepsilon = \frac{\kappa_c z \varepsilon}{u_*^3} = \left(1 + 2.5(z/L)^{3/5}\right)^{3/2}. \tag{14}$$

The similarity relationships are known to be site-specific and depend on the aerodynamic parameters of the measurement site (Hounsinou et al. 2022, 2023; Fortuniak et al. 2013). In our analysis, the similarity relationships are only used as a reference to show the qualitative differences between the observations during rainy and non-rainy times, and even so, the relationships show a qualitatively close fit to the observed data from our study site as can be seen from Figs. 5 and 6 later. Therefore, the site-specific nature of these relationships does not influence the results presented here. In addition to the aforementioned MOST similarity relationships, in a very stable boundary layer ($z/L > 1$), turbulence in vertical components are dampened by stratification such that turbulence becomes independent from the ground and this was denoted as z-less stratification (Wyngaard and Cote 1972; Sorbjan 1987; Smedman 1988; Basu et al. 2006; Grachev et al. 2013; Mahrt et al. 2015; Stiperski and Calaf 2017). For the case of stable stratification, we used the z-less values of turbulence statistics as $\Phi_w = 1.28$, $\Phi_u = 2.3$ (Smedman 1988). Note that, the z-less values for the turbulence statistics vary widely in literature, here we used the values that are close to our findings (Basu et al. 2006; Smedman 1988; Sorbjan 1987; Grachev et al. 2016).

3 Results and Discussions

3.1 SBL Modulations by Raindrops

Taylor Reynolds number (Re_λ) was used to compare the turbulence levels under rainy and non-rainy conditions. Bin-averaged Re_λ ($\overline{Re_\lambda}$) for rainy and non-rainy times is shown in Fig. 2a. In this study, rainy times were defined as $R > 2.6$ mm hr^{-1}, which is the limit of moderate rainfall, and the stability condition was set as 0 (neutral) $< z/L <$ 10 (very stable). As can be seen, $\overline{Re_\lambda}$ was found to be higher during rainy times as compared to those during non-rainy times for the first three velocity bins. On the other hand, as the average streamwise wind velocity becomes $\overline{u} > 2.0$ m s^{-1}, $\overline{Re_\lambda}$ during rainy times becomes less than those during non-rainy times (see Fig. 2a). This may indicate that, as the wind velocity increases, raindrops transition from being a source to being a sink of turbulence in the SBL. Note that while bin-averaged wind speeds for rainy and non-rainy conditions have differences, the differences are small (< 0.1 m s^{-1}) and would not alter the results.

A two-sample t-test with a 0.05 significance level was performed to assess the statistical significance of the absolute difference in $\overline{Re_\lambda}$ between rainy and non-rainy times for each $\overline{u}$ bin. In this test, the null hypothesis was defined as $\left|\overline{Re_\lambda}^R - \overline{Re_\lambda}^{NR}\right| = 0$, where $||$ denotes the absolute value, and the superscripts R and NR denote rainy and non-rainy times, respectively. Table 2 provides $\overline{Re_\lambda}$ values and their standard deviations during both times and the calculated p-values for each $\overline{u}$ bin. According to the calculated p-values, the absolute difference in $\overline{Re_\lambda}$ was found to be statistically significant for the first two $\overline{u}$ bins, where turbulence is likely augmented by the presence of raindrops. Furthermore, statistical significance was also found for the last two $\overline{u}$ bins, where turbulence is likely attenuated by the presence of raindrops. The velocity bins in between the first two bins and the last two bins, where the raindrops act both as a source and sink to turbulence energy, most likely experienced a transition. The possible reasons for this are discussed later in this section. Therefore, turbulence strength

Table 2 Bin-averaged turbulent velocities ($\overline{Re_\lambda}$) and standard deviations (σ_{Re_λ}) during rainy ($R > 2.6$ mm hr^{-1}) and non-rainy ($R = 0$) times for different 1-min averaged streamwise wind velocity ($\overline{u}$) bins.

$\overline{u}$	$R > 2.6$ mm hr^{-1}			$R = 0$			p
	$\overline{Re_\lambda}^R$	${\sigma_{Re_\lambda}}^R$	DOF	$\overline{Re_\lambda}^{NR}$	${\sigma_{Re_\lambda}}^{NR}$	DOF	
0.5–1.0	1517	951	11	782	311	27	0.022539
1.0–1.5	1876	698	50	1175	530	86	0.000000
1.5–2.0	2112	738	91	1893	697	41	0.100269
2.0–2.5	2577	819	120	2871	794	33	0.059689
2.5–3.0	3099	956	130	3688	948	27	0.003372
3.0–3.5	3468	870	93	3356	953	25	0.588088
3.5–4.0	3607	748	48	4508	956	18	0.000451
4.0–4.5	4363	955	42	5304	1079	14	0.004109

The p-values of the two-sample t-test are shown, where the statistical significance was sought in absolute difference of $\overline{Re_\lambda}$ values between rainy and non-rainy times. Here, DOF denotes degree of freedom, and the superscripts R and NR denote rainy, and non-rainy times, respectively

during rainfall is expected to increase when the wind velocities are low ($\overline{u} < 2.0$ m s^{-1}) and decrease when the wind velocities are high ($\overline{u} > 3.5$ m s^{-1}).

The reason for turbulence augmentation and attenuation due to raindrops may be explained by the turbulent kinetic energy budget equation given in Eq. (15).

$$\frac{dk}{dt} = P - \varepsilon + \psi_\sigma \tag{15}$$

Here, P is the turbulent production rate, ε is the dissipation rate, and ψ_σ is the power of the surface tension which is related to the rate of change of the surface area of the raindrops ($dA(t)/dt$) (Dodd and Ferrante 2016). Assuming $\mathrm{dA/dt} = 0$ (i.e. ignoring changes in the raindrop shape and size, for example, due to evaporation), the term of ψ_σ vanishes (Rosti et al. 2019). Therefore, k budget would be determined by P and ε. Heavy inertial particles (e.g. raindrops) produce a wake region while they fall and the turbulence kinetic energy may increase in this wake region by more than $O(1)$ due to vortex shedding and wake oscillations (Bagchi and Balachandar 2004; Balachandar and Eaton 2010). Another increase in turbulence kinetic energy may be due to an increase in the magnitude of the Reynolds stress by the blocking effect of raindrops on turbulent flow (Caldwell and Elliott 1972; Rosti et al. 2019). Therefore, under rainy conditions, the P term in Eq. (15) consists of blocking and wake contributions of raindrops.

It has been reported that ε values are higher for droplet-laden turbulent flows as compared to those for single-phase turbulence (Lucci et al. 2010; Dodd and Ferrante 2016; Rosti et al. 2019). Dodd and Ferrante (2016) showed that a sudden increase in local dissipation rate, and consequently overall dissipation rate, occurs when droplets are released into turbulent flow (Dodd and Ferrante 2016). The increase of the dissipation rate was found to be proportional to $\mu(\partial u/\partial y)^2$, where $\partial u/\partial y$ is the velocity gradient normal to the droplet interface, and the increase in the ε was higher for the case of higher particle inertia (Dodd and Ferrante 2016). Under homogenous shear turbulence as in the SBL, Rosti et al. (2019) found that droplets cause approximately similar amounts of increase in the turbulence production rate due to

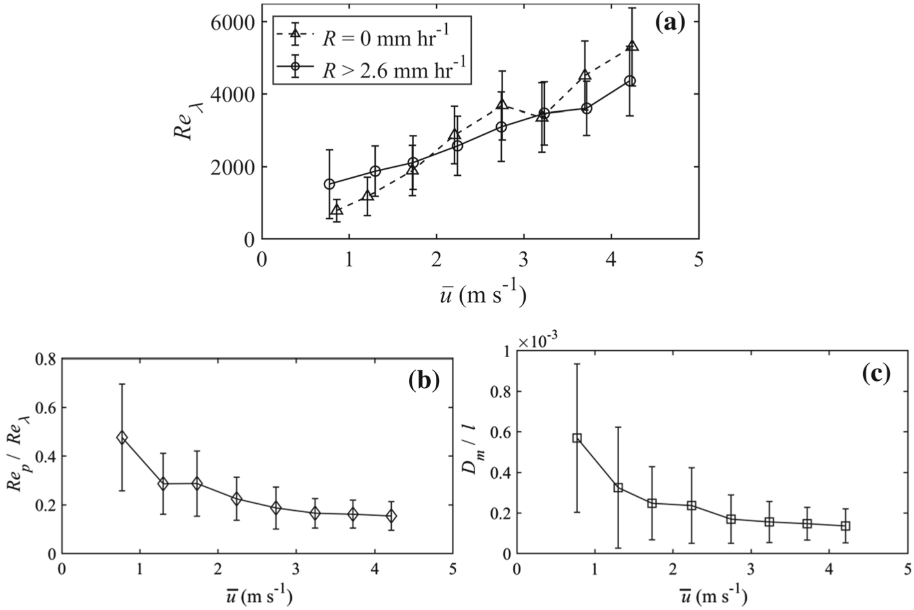

Fig. 2 **a** Bin-averaged Taylor Reynolds number (Re_λ) during rainy (R > 2.6 mm hr^{-1}) (open circles) and non-rainy ($R = 0$) (open triangles) conditions as a function of average streamwise wind velocity bins ($\overline{u}$). Variations of the bin-averaged ratio of particle Reynolds number (Re_p) to Taylor Reynolds number (Re_λ), **b** and mean volume diameter (D_m) to integral length scale (l), **c** as a function of average streamwise wind velocity. Vertical lines represent standard deviations

Reynolds stresses and in the dissipation rate due to velocity gradients. As such, the increase in the turbulence production rate due to Reynolds stresses may balance the increase in the dissipation rate to some extent under rainy conditions. However, the turbulence production due to raindrop wake may result in an elevated turbulence level in the SBL, which may lead to an increased dissipation rate that counters the turbulence production when the equilibrium is restored (see Eq. 15). Turbulence modulation in the wake region may depend on the particle Reynolds number ($\mathrm{Re_p}$) and the surrounding turbulence. Bagchi and Balachandar (2004) observed significant local turbulence enhancement in the wake region of a single stationary particle subject to an isotropic turbulent field when background turbulence intensity was relatively low (10%). They further found that the turbulence level in the wake region was reduced or only slightly increased when the turbulence intensity in the background flow was relatively high (25%). Note that the flow configuration in the study by Bagchi and Balachandar (2004) is different than the fall of raindrops in the atmospheric boundary layer considered in our study. Bagchi and Balachandar (2004) kept the relative velocity between the particle and mean flow fixed and used this relative velocity (instead of $\overline{\mathrm{u}}$ used in our study) to define the turbulence intensity. Therefore, their results may not directly apply to our observations, yet their insights are important to discuss here. In their study, $\mathrm{Re_p}$ values ranged between 50 and 600, corresponding to raindrops with D of 0.5–1.6 mm falling with the corresponding terminal speeds ($\mathrm{v_t}$). Bagchi and Balachandar found that, for the particles with high $\mathrm{Re_p}$, the turbulence enhancement was related to vortex shedding, and for the particles with low $\mathrm{Re_p}$, it was related to wake oscillations. They further showed that the disruption in the vortex shedding and wake oscillations is responsible for the reduced or slightly increased turbulence level in the wake region when the turbulence intensity in the background flow was relatively high (25%). In addition, Ren et al. (2020) found that, wake recirculation region of a drop shortens under turbulent flow conditions as compared to that under still air condition. Furthermore, Ren et al. (2020) reported an increase in turbulent kinetic energy in the wake region of water drops with 2.0 and 3.0 mm in diameter under low turbulence intensity conditions (10%). Based on the findings of these previous studies, augmentation and attenuation of turbulence observed in our study is likely due to wake oscillations and vortex shedding of raindrops during low and high wind speeds, respectively. As indications of the relative importance of raindrop wake conditions to the ambient turbulent flow conditions, we provide the ratio of the $\mathrm{Re_p}$ and $\mathrm{Re_\lambda}$ for all $\bar{\mathrm{u}}$ bins in Fig. 2b. Here, $\mathrm{Re_p}$ was used to represent the wake conditions due to the raindrop size and fall velocity effects (i.e. wake oscillation or vortex shedding) and $\mathrm{Re_\lambda}$ was used to represent the turbulence strength of the ambient flow. Here, for $\mathrm{Re_p} = \mathrm{D_m v_t}/\vartheta$ calculations, $\mathrm{v_t}$ values were calculated using Atlas et al.'s (1973) terminal speed parameterization $\mathrm{v_t} = 9.65 - 10.3 \times \mathrm{e^{-0.6D}}$ (in m $\mathrm{s^{-1}}$) with $D = D_\mathrm{m}$ (in mm), which is valid for $0.6 < D < 5.8$ mm (Testik and Barros 2007). Since D_m was used to calculate both v_t and Re_p, Re_p in here can be considered as the mean volume particle Reynolds number. Considering raindrop D ranging from ~ 0.1–5.8 mm, Re_p values are between ~ 1.8–3549 (Gunn and Kinzer 1949). As can be seen in Fig. 2b, the ratio of Re_p/Re_λ monotonically decreased with increasing wind speed. This is mainly due to increasing Re_λ with increasing $\bar{u}$. Therefore, as the carrier fluid's turbulence increases (i.e. Re_λ), the effect of raindrop vortex shedding and wake oscillations becomes less important, and after a certain level, raindrops start acting as a sink rather than a source of turbulence.

Figure 2c presents the ratio of D_m to l, where l represents the integral length scale of the carrier fluid, to demonstrate the scale relationship between raindrops and the carrier fluid. Here, l was calculated using the streamwise autocorrelation coefficient. As can be seen for the first two $\bar{\mathrm{u}}$ bins, the bin-averaged D_m/l ratios are higher than 0.3×10^{-3}, where turbulence was observed to be significantly higher during rainy times than non-rainy times. On the other hand, when the bin-averaged D_m/l ratios are lower than 0.15×10^{-3}, turbulence was observed to be significantly less during rainy times than non-rainy times. While these D_m/l values do not match with the cut-off D/l value of 0.1 suggested by Gore and Crowe (1991) (i.e. turbulence enhances when $D/\mathrm{l} > 0.1$, and turbulence attenuates when $D/\mathrm{l} < 0.1$), there is a qualitative agreement between our observations and Gore and Crowe's criterion. A direct quantitative comparison for D_m/l values for turbulence enhancement and reduction cut-off values cannot be made with Gore and Crowe's cut-off value as their finding is for single drop sizes whereas our investigation involves the distribution of different raindrop sizes. Furthermore, turbulence modulation is also dependent on other factors such as $\mathrm{Re_p}$ and mass fraction (i.e. ratio of water mass to air mass within a unit cubic volume) (Balachandar and Eaton 2010; Tanaka and Eaton 2010), and the differences in the mass fraction and $\mathrm{Re_p}$ values for the case of rainfall than those for other problems hinder direct comparisons with the reported results in the literature. For instance, $\mathrm{Re_p}$ considered in the literature was around O(1)–O(2); however, for rainfall, $\mathrm{Re_p}$ around O(3) (for $\mathrm{D} > 2.4$ mm) can be commonly observed. Furthermore, the mass fraction in our study ranged between 0.00019 and 0.0088, and it might contribute to the variations in the observed turbulence characteristics than those in numerical and laboratory-based studies. Note that, to calculate the mass fraction values, we used the liquid water content (LWC) parameter. LWC is the volume of all raindrops that are present within a unit volume of air column at a given instant (see, for example, Testik and Pei 2017). LWC information along with rainwater density (approximated as 1000 kg $\mathrm{m^{-3}}$), air density (approximated as 1.225 kg $\mathrm{m^{-3}}$), and air volume within the selected unit volume were used to calculate the mass fraction of rainwater to air. While R is not directly involved in the mass fraction calculations, given their intrinsic relations, the minimum and maximum mass fraction values approximately correspond to the times when minimum and maximum R values of 2.6 and 120 mm hr^{-1}, respectively, were observed in our field campaign.

To further investigate the effect of Re_p on turbulence strength in SBL, we divided the data by turbulence intensity as $TI < 0.31$ (low TI) and $TI > 0.31$ (high TI), where 0.31 was both the mean and the median value of the entire dataset. While a lower TI threshold value may be preferable in general, in this study, the TI threshold value of 0.31 was selected for high and low TI categorizations due to the size and distribution of the data set. The raindrops with a D smaller than 1.0 mm are expected to fall with a steady wake and without noticeable deformation in their shape (Testik and Barros 2007; Feng and Beard 2011). Recent field measurements showed that the raindrops may fall significantly faster or slower than predicted terminal speeds under different environmental conditions including wind and atmospheric turbulence (Montero-Martinez et al. 2009, Montero-Martinez and Garcia-Garcia 2016, Bringi et al. 2018; Testik and Bolek 2023). In our calculations for the $\mathrm{Re_p}$ values, predicted terminal speeds of the corresponding $\mathrm{D_m}$ values were used. Therefore, in investigating the effect of $\mathrm{Re_p}$, we further divided our data into two categories. Since raindrop size is the sole parameter that determines the predicted values of the terminal speed (see Atlas et al.'s terminal speed parameterization provided earlier), $\mathrm{Re_p}$ effects indeed represent raindrop size effects (recall $\mathrm{Re_p} = D_\mathrm{m}\mathrm{v_t}/\vartheta$) and the categorization can be considered in terms of raindrop sizes. The two data categories were: large raindrops for $\mathrm{Re_p} > 528$ and small raindrops for $\mathrm{Re_p} < 528$, where $\mathrm{Re_p} = 528$ corresponds to raindrops with $D = 1.5$ mm. Note that classifying the data into two broad categories instead of many finer categories enabled us to overlook potential inaccuracies in $\mathrm{Re_p}$ calculations in our interpretations. Particularly, while raindrops were assumed to fall at the predicted terminal speeds in our $\mathrm{Re_p}$ calculations, raindrop fall speeds may deviate from the predicted terminal speeds as discussed earlier, especially during wind and turbulence as shown by Testik and Bolek (2023). As such, our choice of data categorization for broad raindrop size ranges made potential fall speed deviations from the terminal speeds insignificant for our analysis purposes and enabled us to account for the wake and shape effects more conservatively. The results are shown in Fig. 3a, and b for low and high TI, respectively. Here, for the sake of clarity of the graphs, only the standard deviations of $\mathrm{Re_p} < 528$ were shown. The standard deviations of data with $\mathrm{Re_p} > 528$ are on the same order of magnitude. As can be seen, under low TI conditions, the average Re_λ for large raindrops ($Re_p > 528$) was higher or almost equal to those for small raindrops ($Re_p < 528$). On the other hand, under high TI conditions, Re_λ values for small raindrops ($Re_p < 528$) were higher than those large raindrops ($Re_p > 528$) for the larger $\overline{u}$ bins ($\overline{u} > 2.5$ m s^{-1}).

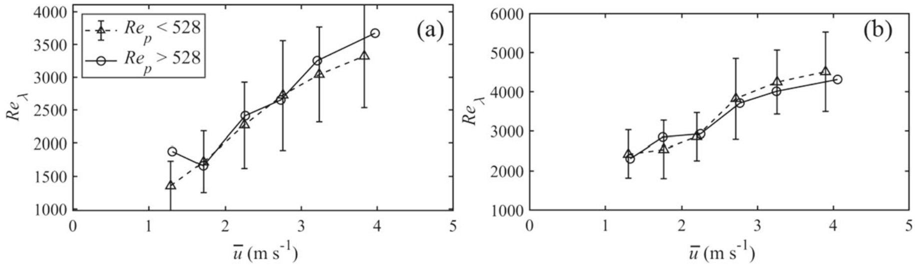

Fig. 3 Variations of bin-averaged Taylor Reynolds number (Re_λ) for **a** $TI < 0.31$ and **b** $TI > 0.31$ as a function of bin-averaged streamwise wind velocity ($\overline{u}$). Vertical lines represent standard deviations for $Re_p < 528$. Here, the last two $\overline{u}$ bins were combined to ensure sufficient data

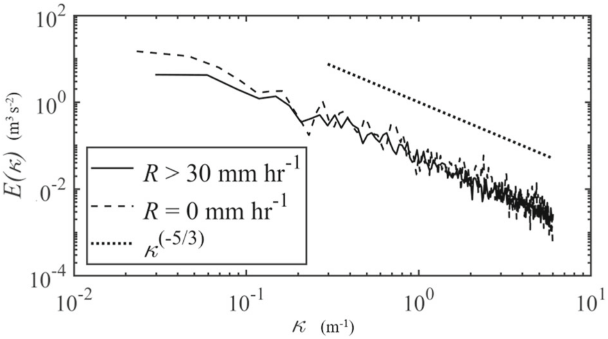

Fig. 4 Energy spectra ($E(\kappa)$) during intense rainy ($R > 30$ mm hr^{-1}, solid line) and non-rainy ($R = 0$ mm hr^{-1}, dashed line) times. The dotted line represents $\kappa^{-5/3}$, where κ is the wave number

Spectral characteristics of stable boundary layer turbulence during intense rainy times were compared with those of non-rainy times in Fig. 4. Here, data was filtered to include only data for $z/L > 0.02$ to discard near-neutral conditions and $R > 30$ mm hr^{-1} to consider only intense rainy times following Caldwell and Elliott (1972). For the data presented in this figure, the average value of R was 42 mm hr^{-1} and the mass fraction value during such R conditions was approximately 0.003. Previous studies have shown that the effects of droplets on turbulence are to augment energy at high wavenumbers in the turbulent energy spectra when the sizes of droplets are on the same order as the Taylor length scale of the carrier fluid (Lucci et al. 2010; Dodd and Ferrante 2016; Rosti et al. 2019; Crialesi-Esposito et al. 2021). This was explained by the break-up of larger eddies due to droplet presence and the creation of new smaller-size eddies (Lucci et al. 2010; Dodd and Ferrante 2016). Crialesi-Esposito et al. (2021) further showed that, due to droplet effects, energy was transferred from low to high wavenumber parts of the spectra with the amount of energy transfer being correlated with the volume fraction. In Fig. 4, the energy spectrum for rainy times was computed as the median of 1-min datasets that have $R > 30$ mm hr^{-1} using 34 1 min datasets. The mean streamwise velocity of these 34 1 min datasets was found as 4.05 ± 2.1 m s^{-1}. The energy spectrum for non-rainy times was computed as the median of 8 1-min datasets. Each of these 8 1-min datasets was chosen to have the streamwise velocity of $U > 3.4$ m s^{-1} with an average streamwise velocity of 4.10 ± 0.44 m s^{-1} for the 8 1 min dataset to approximately match the average streamwise velocity and corresponding turbulence characteristics (i.e., u_* and TI) of rainy and non-rainy times. As a result of this selection, the datasets for the rainy and non-rainy times were comparable with the average u_* and TI values being 0.542 ± 0.273 m s^{-1} and 0.293 ± 0.066 for rainy times and 0.556 ± 0.167 m s^{-1} and 0.337 ± 0.065 for non-rainy times, respectively. Energy spectra were computed as $S_u(n)n = \kappa E(\kappa)$, where $\kappa = 2\pi n/\overline{u}$ is the wavenumber and $E(\kappa)$ is the energy represented in terms of the wavenumber (Piper and Lindquist 2004). As can be seen in this figure, higher energy was observed in the low wavenumber part of the spectra during non-rainy times as compared to the intense rainy times. Although this finding is similar to the findings of Crialesi-Esposito et al. (2021) where the energy in low wavenumber part of the spectra with droplets was found lower than the single-phase spectra, it needs to be further investigated. This is because, in our study, the scale separation is very broad, and the low wavenumber part of the spectra, where rainy and non-rainy spectra show the difference, represents eddies with length scales of approximately 5–50 m and the ratio of D_m/l_η ranges approximately between 1.5–8.0. Considering that eddies should have a similar length scale as the raindrop diameter to break up due to raindrop presence and that D_m was between 1.4–2.75 mm during our intense rainy times observations, the presence of raindrops cannot lead to the breakup of large-scale vortices and the lower energy at the low wavenumber part of the spectra observed during rainy times might be simply due to noise. Although raindrop sizes are much smaller compared to the largest eddies that were observed during intense rainy times, these eddies may lose their energy by a group of vertically falling raindrops, which may explain the observation of lesser energy for rainy times as compared to non-rainy times at low wavenumbers. This mechanism, defined by a series of particles continuously falling through turbulence and causing distortions in the large energetic eddies, has been known as the 'screen effect' (Hwang and Eaton 2006; Tanaka and Eaton 2010). However, presence of this mechanism cannot be confirmed without resolving the high wavenumber part of the spectra. The ejected energy from the low wavenumber part of the spectra should be visible at the high wavenumber part (at least one order higher) to conclude this finding. To resolve the high wavenumber parts, additional observations using anemometers with fast sampling rates are required.

3.2 Near Surface Similarities During Rainfall

As shown in the previous sub-section, turbulence in the SBL may be modulated during rainfall. Therefore, the question arises whether the near-surface similarities are still valid when the boundary layer turbulence is modified by raindrops. In this sub-section, we compared the scaling relationships of rainy ($R > 2.6$ mm hr^{-1}) and non-rainy ($R = 0$ mm hr^{-1}) times where the near-neutral cases ($0 < z/L < 0.02$) were disregarded which restricts the data to only stable cases to reduce the scatter. Figure 5a and b show the bin-averaged normalized standard deviations of the streamwise (Φ_u) and vertical velocity (Φ_w) components as a function of the stability parameter (z/L), respectively. Here, horizontal dashed lines represent the z-less limits provided by Smedman (1988) and solid lines represent the scaled relationships given by Stiperski et al. (2019). As can be seen in Fig. 5a, Φ_u values during non-rainy times roughly follow the z-less similarity for the entire stability ranges, whereas, during rainy times ($R > 2.6$ mm hr^{-1}), Φ_u values start to deviate from the z-less parameter and increase with the stability parameter, especially when the $z/L > 0.15$ (stable). Furthermore, Φ_w values rather closely follow the scaled relationships by Stiperski et al. (2019), during rainy times, whereas they follow the z-less limit during non-rainy times. Furthermore, similar to the case of Φ_u—z/L relationship, the difference in Φ_w values between rainy and non-rainy times becomes larger as the boundary layer gets closer to the very stable limit.

A two-sample t-test with a 0.05 significance level was conducted to evaluate the statistical significance of the absolute difference in $\overline{\Phi_w}$ between rainy and non-rainy times for each z/L bin. In this test, the null hypothesis was defined as $\left|\overline{\Phi_w}^R - \overline{\Phi_w}^{NR}\right| = 0$. Table 3 provides $\overline{\Phi_w}$ values and their standard deviations during both rainy and non-rainy times, and the calculated p-values for each z/L bin. Based on the p-values, the absolute differences between $\overline{\Phi_w}$ values during rainy and non-rainy times were statistically significant for only two z/L bins ($z/L \sim 0.3$ and 2.0). For the rest of the z/L bins, the test failed to reject the null hypothesis mainly due to the large scatter in the data. A large scatter of $\overline{\Phi_w}$ values in the SBL was also reported in the literature, and treatments for this scatter were suggested based on isotropy condition and flux Richardson number (Stiperski and Calaf 2018; Grachev et al. 2013), however, the application of these treatments is out of the scope of this study. Although not shown here, another two-sample t-test with a null hypothesis of $\left|\overline{\Phi_u}^R - \overline{\Phi_u}^{NR}\right| = 0$ was applied, and the

Table 3 Bin-averaged turbulent velocities ($\overline{\Phi_w}$), and standard deviations (σ_{Φ_w}) during rainy ($R > 2.6$ mm hr^{-1}) and non-rainy ($R = 0$) times for different *z/L* parameters.

z/L	$R > 2.6$ mm hr^{-1}			$R = 0$			p
	$\overline{\Phi_w}^R$	$\sigma_{\Phi_w}{}^R$	DOF	$\overline{\Phi_w}^{NR}$	$\sigma_{\Phi_w}{}^{NR}$	DOF	
0.02–0.03	1.310	0.293	79	1.291	0.288	20	0.782445
0.03–0.04	1.307	0.294	55	1.257	0.182	14	0.419937
0.04–0.05	1.372	0.336	51	1.304	0.162	18	0.259769
0.05–0.1	1.406	0.275	150	1.356	0.287	22	0.433829
0.1–0.15	1.459	0.330	65	1.473	0.477	11	0.920351
0.15–0.2	1.577	0.423	24	1.492	0.405	15	0.522411
0.2–0.5	1.775	0.729	47	1.417	0.440	33	0.007133
0.5–1.0	1.725	0.642	17	1.439	0.314	29	0.091709
1.0–10	2.325	0.888	13	1.607	0.697	46	0.007252

The *p*-values of the two-sample t-test is shown where the statistical significance was sought for the difference of $\overline{\Phi_w}$ between rainy and non-rainy times. Here, *DOF* denotes the degree of freedom, and superscripts *R* and *NR* denote rainy and non-rainy times, respectively

difference between rainy and non-rainy times was found to be statistically significant again only for two *z/L* bins (*z/L* ~ 0.18 and 2.0). Even though it failed to reject the null hypothesis for most *z/L* bins, considering the large scatter of the SBL, the scaling functions for the Φ_u and Φ_w deviate during rainfall, especially when $z/L > 0.15$. These deviations may be related to the blocking effect of raindrops, which increases magnitude of the Reynolds stresses (e.g. Rosti et al. 2019), and these effects are expected to become more pronounced as turbulence in SBL weakens.

Finally, we investigated the effect of rainfall on the bin-averaged dimensionless dissipation rate (Φ_ε) (see Fig. 6). Observed Φ_ε values were larger during rainy times ($R > 2.6$ mm hr^{-1}) than during non-rainy times ($R = 0$). The increase in dissipation rate due to particle presence (i.e., droplets in turbulent flows) has been reported previously and was related to an increase in velocity gradients close to the particle interface (Dodd and Ferrante 2016). During $R = 0$, Φ_ε values followed predictions of the similarity relationships by Grachev et al. (2016) (dotted line in Fig. 6a) and by Wyngaard and Cote (1971) (solid line in Fig. 6a). While, in general, observed Φ_ε values and predictions of the similarity relationships were in good agreement, the deviations between them increased with increasing *z/L* values.

4 Conclusions

In this study, rainfall effects on the stable boundary layer in terms of turbulence strength and near-surface similarities were investigated. Microphysical and bulk characteristics of rainfall including raindrop diameter, fall speed, and rainfall rate were measured using Parsivel^2 disdrometer whereas a 3D ultrasonic anemometer (RM-Young 81,000) was used to measure the wind and turbulence characteristics. Rainy data was collected during 26 independent rainfall events that occurred between May 2019 and December 2021, corresponding to a total of 4197 min of data while non-rainy data corresponds to 1280 min of data.

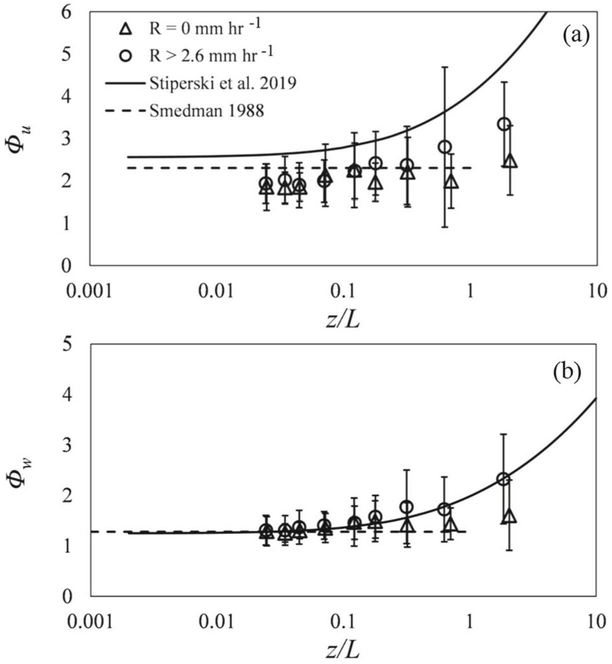

Fig. 5 The relationship between bin-averaged normalized standard deviations of streamwise (Φ_u) **a** and vertical velocity (Φ_w), **b** components and stability parameter (*z/L*) (see Table 3 for the selected z/L bins). The horizontal dashed lines are the *z*-less values proposed by Smedman 1988, whereas the solid lines are the scaled relationships with *z/L* given by Stiperski et al. 2019. The rainy and non-rainy times are denoted by open circles and triangles, respectively. The vertical bars represent the standard deviations

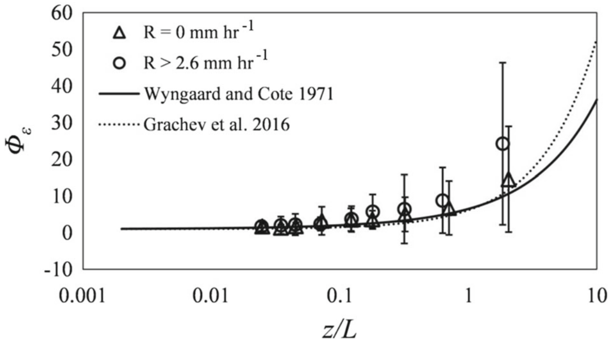

Fig. 6 Bin-averaged normalized dissipation rate (Φ_ε) as a function of stability parameter (*z/L*). The solid line is the scaled relationship with *z/L* by Wyngaard and Cote 1971 and the dotted line is the scaled relationship by Grachev et al. 2016. Rainy and non-rainy times were denoted as open circles and triangles, respectively. Vertical bars represent standard deviations

Our investigation showed that, during rainfall, turbulence energy in the stable boundary layer was higher when the wind speeds were low. On the contrary, for high wind speeds, turbulence energy in the stable boundary layer during rainfall was lower than those of non-rainy conditions. Observed alterations in the turbulence energy during rainfall was likely due to the raindrop wake and turbulence interaction. The effect of Re_p on the turbulence was shown by classifying the data as high $TI > 0.31$ and low $TI < 0.31$. It was found that, for $TI > 0.31$ and $\overline{u} > 2.5$ m s^{-1}, turbulence strength was smaller when the $Re_p > 528$ (i.e. rainfall with larger raindrops) than when $Re_p < 528$ (i.e. rainfall with smaller raindrops). These findings further demonstrate that rainfall modulates turbulence energy in the stable boundary layer, which depends on the Re_p, Re_λ, and TI. Furthermore, we found that turbulence energy at low wavenumbers in the composed spectra during rainfall is lower than those during non-rainy times. This was related to the screen effect, which explains the loss of energy due to the deformation of the large eddies by the continuous fall of raindrops. On the other hand, the difference in the low wavenumber part of the spectra is not distinct and may be related to noise. To verify the effect of the raindrops on the turbulent energy in the stable boundary layer, the high wavenumber part of the spectra also needs to be resolved.

Profound effects of rainfall on near-surface scaling parameters of the stable boundary layer were also observed. It was found that Φ_u and Φ_w follow the z-less similarity during non-rainy times whereas, during rainy times, they deviate from the z-less similarity especially when the boundary layer gets more stable ($z/L > 0.3$). These Φ_u and Φ_w deviations were likely related to the increased Reynolds stresses due to the blocking effect of raindrops on the turbulent air (Rosti et al. 2019). The dimensionless dissipation rate, Φ_ε, was also observed to increase under rainy conditions as compared to non-rainy conditions. During both non-rainy and rainy times, Φ_ε followed the MOST relationship; however, under more stable boundary layer conditions ($z/L > 0.3$), deviations occurred, and the discrepancy between the rainy and non-rainy times Φ_ε increased with z/L. These findings indicate that the similarity functions might have additional dependencies under rainy conditions.

The results of this study show that rainfall modulates turbulence in the stable boundary layer, especially when the turbulence strength in the boundary layer is relatively weak (z/L > 0.5). Turbulence production is likely modified due to increased Reynolds stresses and raindrop wake oscillations and vortex shedding, whereas the dissipation term is likely modified by velocity gradients near the raindrop interface. Further investigation using anemometers with a high sampling rate that can resolve high wave number parts of the energy spectra is needed to clarify the effects of raindrops on the stable boundary layer turbulence. In addition to spike removal, a more specialized quality criteria needs to be developed to effectively assess the impact of the rainfall on the ultrasonic anemometer performance. Even though with strict quality criteria that were imposed in this study, a certain amount of data may still be under the influence of the rainfall. Furthermore, the effect of the rainfall on the heat flux also needs to be investigated since raindrops are expected to increase the vertical mixing in the boundary layer as they fall with relatively high speeds and at different temperatures than surrounding fluid.

Acknowledgements This research was supported by the funds provided by the National Science Foundation under Grants No. AGS-1741250 to the second author (FYT). The first author was a graduate student under the guidance of FYT and is now at Max Planck Institute for Biogeochemistry.

Author Contributions A.B. collected and analyzed the data, and prepared the initial draft of the manuscript and figures. F.Y.T. conceptualized and supervised the research activities and methodology, reviewed and edited the manuscript, and managed the overall project.

Funding The funding provided by the National Science Foundation (Grants No. AGS-1741250)

Data Availability Data presented in this article will be made available upon reasonable request from the corresponding author (Dr. Firat Y. Testik) and after completion of a Fair Use Agreement.

Declarations

Conflict of interest The authors declare no competing interests.

References

Albertson JD, Parlange MB, Kiely G, Eichinger WE (1997) The average dissipation rate of turbulent kinetic energy in the neutral and unstable atmospheric surface layer. J Geophys Res Atmos 102:13423–13432

Atlas D, Srivastava RC, Sekhon RS (1973) Doppler radar characteristics of precipitation at vertical incidence. Rev Geophys 11(1):1–35

Aylor DE, Ducharme KM (1995) Wind fluctuations near the ground during rain. Agric for Meteorol 76(1):59–73. https://doi.org/10.1016/0168-1923(94)02211-2

Bagchi P, Balachandar S (2004) Response of the wake of an isolated particle to an isotropic turbulent flow. J Fluid Mech 518:95–123

Balachandar S, Eaton JK (2010) Turbulent dispersed multiphase flow. Annu Rev Fluid Mech 42:111–133

Basu S, Porté-Agel F, Foufoula-Georgiou E, Vinuesa JF, Pahlow M (2006) Revisiting the local scaling hypothesis in stably stratified atmospheric boundary-layer turbulence: an integration of field and laboratory measurements with large-eddy simulations. Boundary-Layer Meteorol 119(3):473–500

Beljaars ACM (1995) The parametrization of surface fluxes in large-scale models under free convection. Q J R Meteorol Soc 121:255–270. https://doi.org/10.1002/qj.49712152203

Bodini N, Lundquist JK, Newsom RK (2018) Estimation of turbulence dissipation rate and its variability from sonic anemometer and wind Doppler lidar during the XPIA field campaign. Atmos Meas Tech 11:4291–4308. https://doi.org/10.5194/amt-11-4291-2018

Bodini N, Lundquist JK, Krishnamurthy R, Pekour M, Berg LK, Choukulkar A (2019) Spatial and temporal variability of turbulence dissipation rate in complex terrain. Atmos Chem Phys 19:4367–4382. https://doi.org/10.5194/acp-19-4367-2019

Bolek A, Testik FY (2021) Rainfall microphysics influenced by strong wind during a Tornadic storm. J Hydrometeorol. https://doi.org/10.1175/JHM-D-21-0004.1

Boyko V, Vercauteren N (2021) Multiscale shear forcing of turbulence in the nocturnal boundary layer: a statistical analysis. Boundary-Layer Meteorol 179(1):43–72

Bringi V, Thurai M, Baumgardner D (2018) Raindrop fall velocities from an optical array probe and 2-D video disdrometer. Atmos Meas Tech 11:1377–1384. https://doi.org/10.5194/amt-11-1377-2018

Caldwell DR, Elliott WP (1972) The effect of rainfall on the wind in the surface layer. Boundary-Layer Meteorol 3:146–151. https://doi.org/10.1007/BF02033915

Chamecki M, Dias NL (2004) The local isotropy hypothesis and the turbulent kinetic energy dissipation rate in the atmospheric surface layer. Q J R Meteorol Soc 130:2733–2752. https://doi.org/10.1256/qj.03.155

Conry P, Kit E, Fernando HJ (2020) Measurements of mixing parameters in atmospheric stably stratified parallel shear flow. Environ Fluid Mech 20(5):1177–1197

Crialesi-Esposito M, Rosti ME, Chibbaro S Brandt L (2021) Modulation of homogeneous and isotropic turbulence in emulsions. arXiv preprint arXiv:2108.08722

Dodd MS, Ferrante A (2016) On the interaction of Taylor length scale size droplets and isotropic turbulence. J Fluid Mech 806:356–412. https://doi.org/10.1017/jfm.2016.550

Dyer A (1974) A review of flux-profile relationships. Boundary-Layer Meteorol 7:363–372

Feng JQ, Beard KV (2011) Raindrop shape determined by computing steady axisymmetric solutions for Navier–Stokes equations. Atmos Res 101(1–2):480–491

Foken T, Napo CJ (2008) Micrometeorology. Springer, Berlin

Foken T, Wichura B (1996) Tools for quality assessment of surface-based flux measurements. Agric for Meteorol 78(1–2):83–105

Fortuniak K, Pawlak W, Siedlecki M (2013) Integral turbulence statistics over a central European city centre. Boundary-Layer Meteorol 146:257–276

Garratt JR (1994) The atmospheric boundary layer. Earth Sci Rev 37(1–2):89–134. https://doi.org/10.1016/0012-8252(94)90026-4

Gore RA, Crowe CT (1991) Modulation of turbulence by a dispersed phase. J Fluids Eng 113(2):304–307. https://doi.org/10.1115/1.2909497

Grachev AA, Andreas EL, Fairall CW, Guest PS, Persson POG (2013) The critical Richardson number and limits of applicability of local similarity theory in the stable boundary layer. Boundary-Layer Meteorol 147(1):51–82

Grachev AA, Leo LS, Sabatino SD, Fernando HJ, Pardyjak ER, Fairall CW (2016) Structure of turbulence in katabatic flows below and above the wind-speed maximum. Boundary-Layer Meteorol 159(3):469–494

Gunn R, Kinzer GD (1949) The terminal velocity of fall for water droplets in stagnant air. J Atmos Sci 6(4):243–248

Harrison EL, Veron F, Ho DT, Reid MC, Orton P, McGillis WR (2012) Nonlinear interaction between rain- and wind-induced air-water gas exchange. J Geophys Res Ocean 117:1–16. https://doi.org/10.1029/2011JC007693

Högström U (1996) Review of some basic characteristics of the atmospheric surface layer. Boundary-Layer Meteorol 78:215–246. https://doi.org/10.1007/BF00120937

Hogstrom ULF (1988) Non-dimensional wind and temperature profiles in the atmospheric surface layer: a re-evaluation. Top. Micrometeorology. A Festschrift Arch Dye., 55–78

Højstrup J (1981) A simple model for the adjustment of velocity spectra in unstable conditions downstream of an abrupt change in roughness and heat flux. Boundary-Layer Meteorol 21:341–356

Hounsinou M, Mamadou O, Wudba M, Kounouhewa B, Cohard JM (2022) Integral turbulence characteristics over a clear woodland forest in northern Benin (West Africa). Atmos Res 268:105985

Hounsinou M, Mamadou O, Kounouhewa B (2023) Turbulence characteristics in the atmospheric surface layer over a heterogeneous cultivated surface in a tropical region. Boundary-Layer Meteorol 188(2):321–344

Hwang W, Eaton JK (2006) Homogeneous and isotropic turbulence modulation by small heavy () particles. J Fluid Mech 564:361–393

Janjić ZI (1994) The step-mountain eta coordinate model: Further developments of the convection, viscous sublayer, and turbulence closure schemes. Mon Weather Rev 122:927–945

K'ufre-Mfon EE, Hunt FH, Jeffery JL, Otung IE (2015) Modeling rainfall drop size distribution in southern England using a Gaussian mixture model. Radio Sci 50(9):876–885

Kaimal JC (1978) Horizontal velocity spectra in an unstable surface layer. J Atmos Sci 35:18–24

Kaimal JC, Wyngaard JC (1990) The Kansas and Minnesota experiments. Boundary-Layer Meteorol 50:31–47. https://doi.org/10.1007/BF00120517

Kaimal JC, Wyngaard JC, Izumi Y, Coté OR (1972) Spectral characteristics of surface-layer turbulence. Q J R Meteorol Soc 98:563–589

Kaimal JC, and Finnigan JJ (1994) Atmospheric boundary layer flows: their structure and measurement

Kit E, Hocut CM, Liberzon D, Fernando HJS (2017) Fine-scale turbulent bursts in stable atmospheric boundary layer in complex terrain. J Fluid Mech 833:745–772

Liu H, Peters G, Foken T (2001) New equations for sonic temperature variance and buoyancy heat flux with an omnidirectional sonic anemometer. Boundary-Layer Meteorol 100(3):459–468

Lucci F, Ferrante A, Elghobashi S (2010) Modulation of isotropic turbulence by particles of Taylor length-scale size. J Fluid Mech 650:5–55. https://doi.org/10.1017/S0022112009994022

Mahrt L, Sun J, Stauffer D (2015) Dependence of turbulent velocities on wind speed and stratification. Boundary-Layer Meteorol 155(1):55–71

Montero-Martínez G, García-García F (2016) On the behaviour of raindrop fall speed due to wind. Q J R Meteorol Soc 142:2013–2020. https://doi.org/10.1002/qj.2794

Montero-Martínez G, Kostinski AB, Shaw RA, García-García F (2009) Do all raindrops fall at terminal speed? Geophys Res Lett 36:2–5. https://doi.org/10.1029/2008GL037111

Muñoz-Esparza D, Sharman RD, Lundquist JK (2018) Turbulence dissipation rate in the atmospheric boundary layer: observations and WRF mesoscale modeling during the XPIA field campaign. Mon Weather Rev 146:351–371. https://doi.org/10.1175/MWR-D-17-0186.1

Oncley SP, Friehe CA, Larue JC, Businger JA, Itsweire EC, Chang SS (1996) Surface-layer fluxes, profiles, and turbulence measurements over uniform terrain under near-neutral conditions. J Atmos Sci 53:1029–1044. https://doi.org/10.1175/1520-0469(1996)053%3c1029:SLFPAT%3e2.0.CO;2

OTT-Hydromet (2017) Operating instructions present weather sensor OTT Parsivel2. 52 https://www.ott.com/download/operating-instructions-present-weather-sensor-ott-parsivel2-with-screen-heating-1/

Pahlow M, Parlange MB, Porté-Agel F (2001) On Monin-Obukhov similarity in the stable boundary layer. Boundary-Layer Meteorol 99:225–248. https://doi.org/10.1023/A:1018909000098

Park SG, Kim HL, Ham YW, Jung SH (2017) Comparative evaluation of the OTT PARSIVEL 2 using a collocated two-dimensional video disdrometer. J Atmos Oceanic Tech 34(9):2059–2082

Piper M, Lundquist JK (2004) Surface layer turbulence measurements during a frontal passage. J Atmos Sci 61:1768–1780. https://doi.org/10.1175/1520-0469(2004)061%3c1768:SLTMDA%3e2.0.CO;2

Qian Y, Yan H, Berg LK, Hagos S, Feng Z, Yang B, Huang M (2016) Assessing impacts of PBL and surface layer schemes in simulating the surface–atmosphere interactions and precipitation over the tropical ocean using observations from AMIE/DYNAMO. J Climate 29(22):8191–8210. https://doi.org/10.1175/JCLI-D-16-0040.1

Ren W, Reutzsch J, Weigand B (2020) Direct numerical simulation of water droplets in turbulent flow. Fluids 5(3):158. https://doi.org/10.3390/fluids5030158

Rosti ME, Ge Z, Jain SS, Dodd MS, Brandt L (2019) Droplets in homogeneous shear turbulence. J Fluid Mech 876:962–984

Ryzhkov AV, Zrnic DS (2019) Radar polarimetry for weather observations. Springer

Saha R, Testik FY (2023) Assessment of OTT-Parsivel^2 raindrop fall speed measurements. J Atmos Oceanic Tech 40(5):557–573

Smedman AS (1988) Observations of a multi-level turbulence structure in a very stable atmospheric boundary layer. Boundary-Layer Meteorol 44(3):231–253

Sorbjan Z (1987) An examination of local similarity theory in the stably stratified boundary layer. Boundary-Layer Meteorol 38(1):63–71

Stiperski I, Calaf M (2018) Dependence of near-surface similarity scaling on the anisotropy of atmospheric turbulence. Q J R Meteorol Soc 144(712):641–657

Stiperski I, Calaf M, Rotach MW (2019) Scaling, anisotropy, and complexity in near-surface atmospheric turbulence. J Geophys Res Atmos 124(3):1428–1448

Tanaka T, Eaton JK (2010) Sub-Kolmogorov resolution partical image velocimetry measurements of particle-laden forced turbulence. J Fluid Mech 643:177–206

Testik FY, Barros AP (2007) Toward elucidating the microstructure of warm rainfall: a survey. Rev Geophys. https://doi.org/10.1029/2005RG000182

Testik FY, Bolek A (2023) Wind and turbulence effects on raindrop fall speed. J Atmos Sci 80(4):1065–1086

Testik FY, Pei B (2017) Wind effects on the shape of raindrop size distribution. J Hydrometeorol. https://doi.org/10.1175/JHM-D-16-0211.1

Vickers D, Mahrt L (1997) Quality control and flux sampling problems for tower and aircraft data. J Atmos Ocean Technol 14:512–526. https://doi.org/10.1175/1520-0426(1997)014%3c0512:QCAFSP%3e2.0.CO;2

Wilczak JM, Oncley SP, Stage SA (2001) Sonic anemometer tilt correction algorithms. Boundary-Layer Meteorol 99:127–150. https://doi.org/10.1023/A:1018966204465

Wyngaard JC, Coté OR (1971) The budgets of turbulent kinetic energy and temperature variance in the atmospheric surface layer. J Atmos Sci 28:190–201

Wyngaard JC, Coté OR (1972) Cospectral similarity in the atmospheric surface layer. Q J R Meteorol Soc 98(417):590–603

Zhang R, Huang J, Wang X, Zhang JA, Huang F (2016) Effects of precipitation on sonic anemometer measurements of turbulent fluxes in the atmospheric surface layer. J Ocean Univ China 15:389–398